Journal of Magnetic Resonance 208 (2011) 34–43

Contents lists available at ScienceDirect

Journal of Magnetic Resonance

journal homepage: www.elsevier.com/locate/jmr

The displacement correlation tensor: Microstructure, ensemble anisotropy and curving fibers

Sune Nørhøj Jespersen [a,*], Niels Buhl [a,b]

[a] Center of Functionally Integrative Neuroscience, Aarhus University Nørrebrogade 44, Building 10G, 5th floor, Århus, Denmark
[b] Department of Physics and Astronomy, Aarhus University, Ny Munkegade 120, 8000 Århus C, Denmark

ARTICLE INFO

Article history:
Received 26 July 2010
Revised 1 October 2010
Available online 8 October 2010

Keywords:
MRI
Double wave vector diffusion
Curving fibers
Cumulant expansion
Displacement correlations
Surface to volume ratio
Scatter matrix

ABSTRACT

Experiments with multiple diffusion wave vectors are known to carry more information than what is available from standard diffusion experiments. Here we consider a special case of this class of pulse sequences, the double wave vector diffusion experiment, and use the cumulant expansion of the signal to introduce the displacement correlation tensor. We discuss its physical interpretation and properties, noting in particular that its short time behavior allows determination of the surface to volume ratio of the pore space. We present a general expression for the displacement correlation tensor, and provide explicit expressions for a few model geometries. We then show that the scatter matrix characterizing the orientation distribution of an ensemble of cylinders is simply related to the displacement correlation tensor. This result is generalized to ensembles of pores with arbitrary shapes allowing a precise formulation of the influence of microstructural and ensemble anisotropy on the double wave vector diffusion signal in the Gaussian phase approximation. Finally, as a new application of the double wave vector diffusion signal, we analyze its behavior in a curving fiber, and suggest that the displacement correlation tensor may be used to estimate sub-voxel fiber curvature and deflection angle. The theoretical results are corroborated by computer simulations.

© 2010 Elsevier Inc. All rights reserved.

1. Introduction

Pulsed field gradient diffusion sequences with multiple diffusion encoding blocks have recently gained renewed interest in the magnetic resonance community. Proposed originally in a special case by Cory et al. [1,2] as a means of characterizing compartmental eccentricity, it was soon adapted by Callaghan and coworkers to allow estimation of velocity auto-correlations [3] and the dispersion tensor [4]. Jerschow and Müller [5] suggested its use in suppressing convection artifacts in MR diffusion measurements. Mitra contributed a theoretical analysis [6] of the diffusion signal in the narrow pulse regime focusing mainly on the special case with two independent diffusion encoding blocks, the so-called double wave vector diffusion experiment. He derived an expression demonstrating that the dependence of the diffusion signal at low diffusion weighting on the angle between the associated diffusion wave vectors could be used to (i) distinguish a macroscopically isotropic system of anisotropic pores with restricted diffusion from e.g. systems with a distribution of diffusion coefficients and (ii) estimate the size of confining pores. These properties continue to inspire a large part of current research on multiple wave vector diffusion. On the experimental side, Koch and Finsterbusch [7] and Komlosh et al. [8] provided some early demonstrations on biological samples, and the former group has recently obtained promising results in the human corticospinal tract *in vivo* [9]. A number of studies have been performed on phantoms [10–12] and biological tissue, including gray matter [13] and spinal cord [14–16]. These experimental results generally lend encouragement to the feasibility of the theoretical predictions first put forth by Mitra.

Özarslan and Basser studied diffusion–diffraction phenomena in the setting of multiple pulsed field gradient experiments [17], and suggested an approach which has subsequently been demonstrated to provide a robust determination of pore sizes [18,19], even for polydisperse samples where the diffraction patterns from the single pulse diffusion experiment tend to disappear. In a later series of comprehensive theoretical works [11,20,21], Özarslan and coworkers have extended the framework originally introduced by Barzykin and Grebenkov [22,23] to investigate the behavior of the double pulsed field gradient experiment for diffusion in restricted geometries, allowing a mathematical calculation of the signal in a wide range of model systems and notably for a broad selection of experimental conditions. A point of main focus there has been the sensitivity of the double wave vector diffusion experiment to both microstructural anisotropy (non-spherical pore shapes) and ensemble anisotropy. The latter term refers to an

* Corresponding author. Fax: +45 8949 4400.
E-mail addresses: sune@cfin.au.dk (S. Nørhøj Jespersen), nbuhl@phys.au.dk (N. Buhl).

1090-7807/$ - see front matter © 2010 Elsevier Inc. All rights reserved.
doi:10.1016/j.jmr.2010.10.003

anisotropic orientation distribution of pores with microstructural anisotropy, a problem also considered by Finsterbusch and Koch, who developed a tensor formalism on the basis of a Taylor expansion of the signal in the limit of large diffusion times and zero mixing time [24,25]. By considering the difference between the signals arising from two double wave vector diffusion experiments, one with parallel gradients and one with anti-parallel gradients, they introduced tensors from which microstructural anisotropy and pore size could be characterized.

In this work, we employ the cumulant expansion of the double wave vector diffusion signal and demonstrate its use for determination of the spin displacement correlation tensor. As the diffusion time becomes large and the mixing time is set to zero, this tensor becomes equivalent to the one introduced by Koch and Finsterbusch [24]. We discuss its physical significance and properties, and obtain an expression relating its short diffusion time behavior to the surface to volume ratio of the pore space, analogous to the short time behavior of the diffusion coefficient [26,27]. We present a general expression for the displacement correlation tensor in terms of eigenfunctions, and use it to provide exact expressions for example model geometries. For a collection of long cylinders, we show that the displacement correlation tensor is closely related to the scatter matrix of the cylinder orientation distribution. We then go on to generalize this result to collections of pores of arbitrary shapes, and obtain a simple expression relating the displacement correlation tensor, and in fact the double wave vector diffusion signal in the Gaussian phase approximation, to pore and ensemble characteristics. This result is a precise statement about which aspects of the pore orientation distribution influence the double wave vector diffusion signal, and how it combines with the microstructural anisotropy. Finally we point to a new possible use of the double wave vector diffusion experiment by considering the behavior of the displacement correlation tensor in curved fibers, and show how it could in principle be used to detect sub-voxel fiber curvature and deflection angle.

2. Theory

2.1. Cumulant expansion of the double wave vector diffusion signal

The double wave vector diffusion sequence is illustrated in Fig. 1, where the experimental parameters are defined also. Only the special case of identical diffusion periods ($\Delta_1 = \Delta_2 \equiv \Delta$) will be considered, and we will assume the narrow pulse regime [28] to allow the Fourier relationship in Eq. (1) below. We employ the convention $\boldsymbol{q} = \gamma \boldsymbol{g}\delta$ for the diffusion wave vector, where γ is the gyromagnetic ratio, $\boldsymbol{g}$ the diffusion gradient, and δ its duration. We consider the signal $S(\boldsymbol{q}_1, \boldsymbol{q}_2)$, normalized so $S(0, 0) = 1$, from the double wave vector pulse sequence with diffusion gradients placed at $t_1 = 0$, $t_2 = \Delta$, $t_3 = \Delta + \tau$, and $t_4 = 2\Delta + \tau$, resulting in diffusion wave vectors $\boldsymbol{q}_1$ and $\boldsymbol{q}_2$, and

$$S(\boldsymbol{q}_1, \boldsymbol{q}_2) = \langle e^{-i\mathbf{q}_1\cdot(\mathbf{r}_2-\mathbf{r}_1)-i\mathbf{q}_2\cdot(\mathbf{r}_3-\mathbf{r}_4)}\rangle = \langle e^{-i\mathbf{q}_1\cdot\mathbf{R}_1+i\mathbf{q}_2\cdot\mathbf{R}_2)}\rangle = \langle e^{-i\phi}\rangle, \tag{1}$$

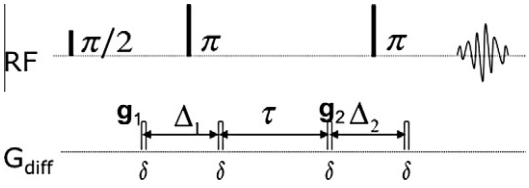

Fig. 1. Illustration of the basic spin echo double wave vector diffusion pulse sequence with pulse sequence parameters $\mathbf{g}_1$ and $\mathbf{g}_2$ (diffusion gradients), δ (gradient duration), Δ_1 and Δ_2 (diffusion times) and τ (mixing time). Here we only consider sequences with $\Delta_1 = \Delta_2$.

where $\boldsymbol{r}_i = \boldsymbol{r}(t_i)$ is the spin position, $\boldsymbol{R}_1$ and $\boldsymbol{R}_2$ are the displacements during the first and second diffusion encoding intervals (e.g. $\boldsymbol{R}_1 = \boldsymbol{r}_2 - \mathbf{r}_1$), and $\phi = \mathbf{q}_1\cdot\mathbf{R}_1 - \mathbf{q}_2\cdot\mathbf{R}_2$ is the spin phase. Angular brackets signify averaging over all spins contributing to the signal. The cumulant expansion is valid for a large class of probability distributions [29,30] and applied to the phase distribution, it reads

$$\log S = \log\langle e^{-i\phi}\rangle = \langle -i\phi\rangle - \frac{1}{2}(\langle\phi^2\rangle - \langle\phi\rangle^2) + \cdots \tag{2}$$

to second order in the diffusion wave vectors. In the absence of coherent motion, we expect $\langle\mathbf{R}_i\rangle = 0$, and so only the second moment contributes to this order:

$$\langle\phi^2\rangle = q_{1\alpha}q_{1\beta}\langle R_{1\alpha}R_{1\beta}\rangle + q_{2\alpha}q_{2\beta}\langle R_{2\alpha}R_{2\beta}\rangle - 2q_{1\alpha}q_{2\beta}\langle R_{1\alpha}R_{2\beta}\rangle, \tag{3}$$

where from here onwards greek letter subscripts label cartesian components and sum over repeated indices is implied (Einstein summation convention)—i.e. $q_{1\alpha}R_{1\alpha} \equiv q_{1x}R_{1x} + q_{1y}R_{1y} + q_{1z}R_{1z}$, etc. It is reasonable to assume that diffusion is a stationary process over the relevant experimental timescales, ensuring that the mean square displacement tensors during the two diffusion encoding blocks are identical, i.e. $\langle R_{1\alpha}R_{1\beta}\rangle = \langle R_{2\alpha}R_{2\beta}\rangle$. Note that for small diffusion times $\Delta \to 0$, $\langle R_{1\alpha}R_{1\beta}\rangle = 2D_{\alpha\beta}\Delta$, where $D_{\alpha\beta}$ is the diffusion tensor. The signal from the double wave vector diffusion sequence in the second-order cumulant expansion (Gaussian phase approximation) thus reads:

$$S = \exp\left(-\frac{1}{2}(q_{1\alpha}q_{1\beta} + q_{2\alpha}q_{2\beta})\langle R_{1\alpha}R_{1\beta}\rangle + q_{1\alpha}q_{2\beta}\langle R_{1\alpha}R_{2\beta}\rangle\right). \tag{4}$$

The tensor

$$\begin{aligned} Q_{\alpha\beta}(\tau,\Delta) &\equiv \langle R_{1\alpha}R_{2\beta}\rangle \\ &= \langle (r_\alpha(0) - r_\alpha(\Delta))(r_\beta(\Delta+\tau) - r_\beta(2\Delta+\tau))\rangle \\ &= \langle r_{1\alpha}r_{3\beta}\rangle + \langle r_{2\alpha}r_{4\beta}\rangle - \langle r_{1\alpha}r_{4\beta}\rangle - \langle r_{2\alpha}r_{3\beta}\rangle \end{aligned} \tag{5}$$

is an explicit measure of correlation between displacements in the two periods, i.e. the displacement correlation tensor, and will be the main focus of this work. Note importantly that it is the correlations in the displacements of a single spin. It can be extracted using pairs of double diffusion wave vector experiments, for example using

$$\frac{\log S(q,q) - \log S(q,-q)}{2} = \mathbf{q}^T\mathrm{Q}\mathbf{q}. \tag{6}$$

In the presence of flow, Eq. (6) can be generalized by taking absolute values of the signal before the logarithm. An analogous result correct to $\mathcal{O}(q^4)$ applies for the Taylor expansion of the signal, and was considered in the special case of $\tau = 0$ and large diffusion times Δ in [24], but we expect the cumulant expansion to have a wider range of applicability, as will be demonstrated below. Next, we note some properties of Q.

2.2. The displacement correlation tensor

In many cases of interest (excluding again flow), the probability of a random walk trajectory does not depend on the direction in which it is traversed, and therefore $\langle R_{1\alpha}R_{2\beta}\rangle = \langle R_{2\alpha}R_{1\beta}\rangle$. It follows that in d dimensions Q is a real, symmetric $d \times d$ matrix, with entries $Q_{\alpha\beta} = \langle R_{1\alpha}R_{2\beta}\rangle$—i.e. the average product of the spin displacements during the two diffusion encoding blocks, see Fig. 2 for an illustration. It can thus be obtained from a minimum of one $q = 0$ experiment, to render the signal normalized, plus 2×6 double diffusion experiments to supply sufficient information to extract the 6 independent components using Eq. (6). A convenient set of diffusion directions can be obtained from conventional DTI acquisition schemes by using two sets of directions in the double wave vector experiments $(\hat{\mathbf{n}}, \hat{\mathbf{n}})$ and $(\hat{\mathbf{n}}, -\hat{\mathbf{n}})$ for each diffusion gradient direction

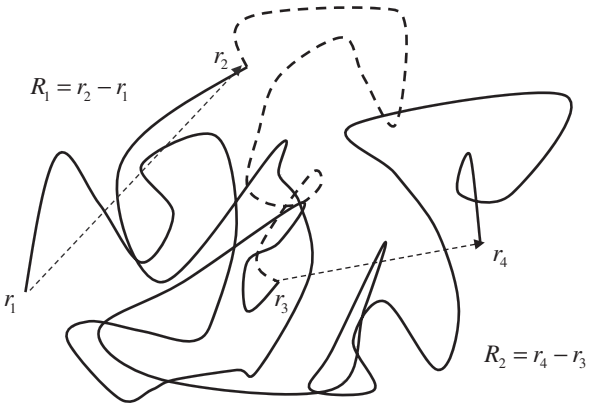

Fig. 2. The relation of $Q_{\alpha\beta} = \langle R_{1\alpha}R_{2\beta}\rangle$ to a random walk trajectory. The solid lines represent the trajectory during the two diffusion encoding blocks, and the dashed line represents the motion during the mixing time.

$\hat{\mathbf{n}}$ in the DTI set. Note that the trace of Q, Tr(Q), can be obtained from 2×3 measurements.

For Markovian diffusion with a Gaussian propagator (Gaussian diffusion), $\mathbf{R}_1$ is independent of $\mathbf{R}_2$, and therefore Q = 0. A nonzero Q thus reflects non-Gaussian diffusion. Moreover, it reflects non-Gaussian properties as induced by microscopic factors, and not merely those that may be a result of ensemble properties, such as from averaging over a distribution of diffusion coefficients. That is, for an ensemble of Gaussian compartments, Q = 0, even though the signal from a single wave vector diffusion experiment need not be mono-exponential. Thus Q can be interpreted as an index of compartmental non-Gaussianity of diffusion. In contrast to the kurtosis [31], a marker of non-Gaussian diffusion, Q can be obtained using low diffusion weighting since it appears already at second order in the cumulant expansion whereas the kurtosis appears at fourth order.

In many situations of interest, correlations are induced mainly by boundaries of a confining pore, e.g. a cell. In this case, reflections (and barriers in general) will tend to cause anti-correlations, and thus Q will be a non-positive definite matrix—see below for a mathematical derivation of this property.

The displacement correlation tensor depends on two timing parameters, the diffusion time $\Delta = t_2 - t_1$ and the "mixing time" $\tau = t_3 - t_2$. In the limit $\Delta \to \infty$, $Q_{\alpha\beta} \to -\langle r_\alpha(\Delta)\, r_\beta(\Delta+\tau)\rangle = -\langle r_\alpha(0)\, r_\beta(\tau)\rangle$, and it can therefore be related to the mean square displacement tensor and the pore "radius of gyration tensor" $\langle r_\alpha r_\beta\rangle$

$$\begin{aligned} Q_{\alpha\beta} &\approx -\langle r_\alpha(0) r_\beta(\tau)\rangle \\ &= -\langle r_\alpha r_\beta\rangle + \frac{1}{2}\langle (r_\alpha(\tau) - r_\alpha(0))(r_\beta(\tau) - r_\beta(0))\rangle. \end{aligned} \tag{7}$$

The validity of this equation is readily confirmed by factoring out the second term on the right-hand side,

$$\begin{aligned} 2D_{\alpha\beta}(\tau)\tau &\equiv \langle (r_\alpha(\tau) - r_\alpha(0))(r_\beta(\tau) - r_\beta(0))\rangle \\ &= \langle r_\alpha(\tau) r_\beta(\tau)\rangle - \langle r_\alpha(0) r_\beta(\tau)\rangle - \langle r_\alpha(\tau) r_\beta(0)\rangle \\ &\quad + \langle r_\alpha(0) r_\beta(0)\rangle \\ &= 2\langle r_\alpha(0) r_\beta(0)\rangle - 2\langle r_\alpha(0) r_\beta(\tau)\rangle \end{aligned} \tag{8}$$

since $\langle (r_\alpha(\tau) r_\beta(0)\rangle = \langle (r_\alpha(0) r_\beta(\tau)\rangle$, and where we have introduced the time-dependent diffusion tensor $D_{\alpha\beta}(t)$. Therefore, in the special case that $\Delta \to \infty$ and $\tau = 0$, $-Q$ simplifies to the radius of gyration tensor also considered in [24].

In the opposite regime, building on Mitra's [26,27] classical result for the short time behavior of the time-dependent diffusion coefficient, it is straightforward to derive the behavior of Tr(Q) in systems with uniform spin density in the limit of a small diffusion time Δ, here reproduced for $\tau = 0$

$$\mathrm{Tr}(\mathrm{Q}) = -S/V \frac{8(\sqrt{2}-1)}{3\sqrt{\pi}} (D\Delta)^{3/2} + \mathcal{O}((D\Delta)^2), \tag{9}$$

where S/V is the surface to volume ratio and $D = \lim_{t\to 0}\mathrm{Tr}(\mathrm{D}(t))$ is the free diffusion constant. This result is a consequence of the fact that the propagator near a reflecting wall is the sum of a Gaussian and its mirror image, but is derived most easily by reexpressing Eq. (5) in terms of sums of mean square displacements and using the result from Mitra et al. [26,27] for the short time behavior of the time-dependent diffusion coefficient. To see this, we use Eq. (8) to rewrite Eq. (5) as follows:

$$\begin{aligned} Q_{\alpha\beta}(\tau,\Delta) &= \langle r_{1\alpha} r_{3\beta}\rangle + \langle r_{2\alpha} r_{4\beta}\rangle - \langle r_{1\alpha} r_{4\beta}\rangle - \langle r_{2\alpha} r_{3\beta}\rangle \\ &= 2D_{\alpha\beta}(\Delta+\tau)(\Delta+\tau) + 2D_{\alpha\beta}(\Delta+\tau)(\Delta+\tau) \\ &\quad - 2D_{\alpha\beta}(2\Delta+\tau)(2\Delta+\tau) - 2D_{\alpha\beta}(\tau)\tau. \end{aligned} \tag{10}$$

Taking the trace of Eq. (10) in the limit $\Delta \to 0$ and with $\tau = 0$, and substituting the results from Mitra et al. [26,27] for the time-dependent diffusion coefficient yields Eq. (9). Thus, like the time-dependent diffusion coefficient, the displacement correlation tensor decreases as a power law in time with the constant of proportionality reflecting the surface to volume ratio, but in contrast to the diffusion coefficient, it decreases from an initial value of zero. The physical origin of this effect is similar to that for the diffusion coefficient, and is due to spins in a boundary layer with volume fraction $S\sqrt{D\Delta}/V$ experiencing displacement correlations on the order of $D\Delta$ due to the reflecting walls. Note that as a consequence of Eq. (10), many of the properties of double wave vector diffusion experiments are reflected in the time-dependent diffusion constant.

The displacement correlation tensor can readily be calculated in any system in which the diffusion propagator $P(\mathbf{r}_2{-}\mathbf{r}_1,t)$ and spin density $\rho(\mathbf{r})$ are known. For example, if the eigenfunctions Ψ_n and eigenvalues λ_n of the diffusion Laplace operator $D\nabla^2$ can be found, we can employ the spectral representation [32] of the propagator

$$P(\mathbf{r}_2|\mathbf{r}_1,t) = \sum_{n=1}^{\infty} e^{-\lambda_n t} \Psi_n^*(\mathbf{r}_1)\Psi_n(\mathbf{r}_2) \tag{11}$$

to express each of the terms in Eq. (5) as

$$\begin{aligned} \langle r_{1\alpha} r_{3\beta}\rangle &= \int d^d r_1 d^d r_3 \rho(bf\mathbf{r}_1) P(\mathbf{r}_3|\mathbf{r}_1, \tau+\Delta) r_{1\alpha} r_{3\beta} \\ &= \sum_{n=1}^{\infty} e^{-\lambda_n(\tau+\Delta)} \int d^d r_1 d^d r_3 \rho(\mathbf{r}_1)\Psi_n^*(\mathbf{r}_1)\Psi_n(\mathbf{r}_3) r_{1\alpha} r_{3\beta} \\ &\equiv \sum_{n=1}^{\infty} e^{-\lambda_n(\tau+\Delta)} S_{\alpha\beta}^{(n)}, \end{aligned} \tag{12}$$

where

$$S_{\alpha\beta}^{(n)} = \int d^d r_1 d^d r_3 \rho(\mathbf{r_1})\Psi_n^*(\mathbf{r}_1)\Psi_n(\mathbf{r}_3) r_{1\alpha} r_{3\beta}.$$

Collecting all the terms in Eq. (5), we find for Q the expression:

$$Q_{\alpha\beta} = -\sum_{n=1}^{\infty} S_{\alpha\beta}^{(n)} e^{-\lambda_n\tau}(1 - e^{-\lambda_n\Delta})^2. \tag{13}$$

It is clear from this equation that in the case of constant spin density $\rho(\mathbf{r})$, the diagonal entries of Q in any coordinate system are non-positive, and thus Q is non-positive definite as noted above.

Using Eq. (13) one may readily calculate exact expressions for Q in model geometries. For example, in the case of diffusion between parallel plates separated by distance a along the z-direction, the only non-zero component of Q is

$$\mathrm{Q}_{zz} = -8a^2 \sum_{m=0}^{\infty} e^{-\alpha_m^2 D\tau/a^2}(1 - e^{-\alpha_m^2 D\Delta/a^2})^2/\alpha_m^4, \tag{14}$$

where $\alpha_m = (2m+1)\pi$. For an infinite cylinder of radius a oriented along the z direction, we find

$$\mathrm{Q} = K\begin{bmatrix}1&0&0\\0&1&0\\0&0&0\end{bmatrix}, \tag{15}$$

where

$$K(\tau,\Delta) = -2a^2\sum_{m=1}^{\infty} e^{-\beta_m^2 D\tau/a^2}(1-e^{-\beta_m^2 D\Delta/a^2})^2/(\beta_m^2(\beta_m^2-1)), 35 \tag{16}$$

and β_m is the mth root of the Bessel function derivative $J_1'(x)$.

2.3. Influence of ensemble and microstructural anisotropy

2.3.1. Cylindrical pores

The anisotropy of the displacement correlation tensor reflects both microscopic and macroscopic anisotropy, and an ensemble of identical cylinders represents a good starting point for discussing the combined influence of microstructural anisotropy and ensemble anisotropy on Q. Consider first a single cylinder oriented along the direction $\hat{\mathbf{u}}$. We would like to express the value of the scalar $\hat{\mathbf{n}}^T\mathrm{Q}\hat{\mathbf{n}}$ for some arbitrary direction $\hat{\mathbf{n}}$. This is most easily evaluated in the coordinate system in which the z-axis is parallel to $\hat{\mathbf{u}}$, and $\hat{\mathbf{n}}$ is in the zx plane at an angle θ to $\hat{\mathbf{u}}$. From Eq. (15) and $\hat{\mathbf{n}} = (\sin\theta, 0, \cos\theta)^T$ it follows immediately that

$$Q(\hat{\mathbf{n}}) \equiv \hat{\mathbf{n}}^T\mathrm{Q}\hat{\mathbf{n}} = K\sin^2\theta = K(1-(\hat{\mathbf{u}}\cdot\hat{\mathbf{n}})^2). \tag{17}$$

In an ensemble of cylinders, the average in Eqs. (1)–(5) can be carried out in two steps by first averaging over spins in a single pore and then averaging over pores. Applied to displacement correlation tensor, the first averaging yields the pore specific Q, and the second averaging the sample Q. Specifying the ensemble of cylinders by their orientation distribution function $f(\hat{\mathbf{u}})$, we can thus readily compute the exact displacement correlation tensor for the entire system by averaging Eq. (17) over cylinder orientations:

$$\begin{aligned} Q(\hat{\mathbf{n}}) &= K\int d\hat{\mathbf{u}} f(\hat{\mathbf{u}})(1-(\hat{\mathbf{u}}\cdot\hat{\mathbf{n}})^2) = K(1-n_\alpha n_\beta\langle u_\alpha u_\beta\rangle_f) \\ &\equiv K(1-\hat{\mathbf{n}}^T\mathrm{T}\hat{\mathbf{n}}). \end{aligned} \tag{18}$$

The subscript on the angular brackets is a reminder that this average is over cylinder orientations. The tensor $T_{\alpha\beta} = \langle u_\alpha u_\beta\rangle_f$ is the explicitly symmetric scatter matrix or orientation matrix [33] of the cylinder orientation distribution, and is a spherical analogue of the second moment. Its eigenvectors specify the main directions in the distribution, and the eigenvalues reflect the scatter around these directions. The trace of the scatter matrix is always 1, and T = I/3 for an isotropic distribution, where I is the identity matrix. Thus we conclude from Eq. (18)

$$\mathrm{Q} = K(\mathrm{I}-\mathrm{T}). \tag{19}$$

This equation shows that microstructural anisotropy as reflected by a nonzero K combines multiplicatively with ensemble anisotropy as expressed by I − T. Also, since T contains five independent elements, both sides of Eq. (19) involve six unknowns and thus these two sources of anisotropy can be separated given a complete measurement of Q. Eq. (19) demonstrates explicitly which aspect of the orientation distribution influences the displacement correlation tensor, and in fact the double wave vector diffusion signal to second order in q, since an analogous relationship can be established for the mean square displacement tensor $\langle R_{1\alpha}R_{1\beta}\rangle$ [34], see below. Note that Tr(Q) = 2K, which can be used to obtain a rotationally invariant measure of the pore size [24]. For later use we note that Eq. (19) implies the existence of simultaneous eigenvectors of Q and T with eigenvalues $\lambda_j^{(\mathrm{Q})}$ and $\lambda_j^{(T)}$, respectively, satisfying:

$$\lambda_j^{(\mathrm{Q})} = K(1-\lambda_j^{(T)}), \quad j = 1,2,3. \tag{20}$$

2.3.2. Arbitrary pore shapes

The result obtained above for cylindrical pores can be extended to apply for general pore shapes and for arbitrary orientation distributions. By expressing the Q corresponding to a single pore in its principal coordinate system specified by eigenvectors $(\hat{\mathbf{u}},\hat{\mathbf{v}},\hat{\mathbf{w}})$,

$$\mathrm{Q} = \begin{bmatrix}A&0&0\\0&B&0\\0&0&C\end{bmatrix} = A\hat{\mathbf{u}}\hat{\mathbf{u}}^T + B\hat{\mathbf{v}}\hat{\mathbf{v}}^T + C\hat{\mathbf{w}}\hat{\mathbf{w}}^T, \tag{21}$$

where A, B and C are the eigenvalues corresponding to $\hat{\mathbf{u}},\hat{\mathbf{v}}$ and $\hat{\mathbf{w}}$, we can average immediately over the distribution of pore orientations to obtain the sample Q:

$$\mathrm{Q} = A\mathrm{T}^{(1)} + B\mathrm{T}^{(2)} + C\mathrm{T}^{(3)}, \tag{22}$$

where $\mathrm{T}^{(i)}$ are the scatter matrices corresponding to each of the pore principal axes; i.e. $T^{(1)}_{\alpha\beta} = \langle u_\alpha u_\beta\rangle_f$, $T^{(2)}_{\alpha\beta} = \langle v_\alpha v_\beta\rangle_f$ and $T^{(3)}_{\alpha\beta} = \langle w_\alpha w_\beta\rangle_f$. Equation (22) applies to arbitrary shapes and orientation distributions, and specifies precisely how microstructural anisotropy and ensemble anisotropy combine to produce the displacement correlation tensor. Moreover, it reveals exactly what aspects of the orientation distribution function are relevant, and it is the second moments encapsulated in the principal directions scatter matrices. Note that the scatter matrices in Eq. (22) are not independent: since the eigenvectors constitute a complete set in $\mathbb{R}^3$, we find the constraint $\mathrm{T}^{(1)} + \mathrm{T}^{(2)} + \mathrm{T}^{(3)} = \mathrm{I}$. Thus, 10 independent numbers are generally required to characterize all three scatter matrices; 5 from each of $\mathrm{T}^{(1)}$ and $\mathrm{T}^{(2)}$, and the constraint above then gives $\mathrm{T}^{(3)}$. Therefore, microstructural and ensemble anisotropy cannot be separated without additional knowledge acquired e.g. from the time dependence of Q. Again, since Eq. (21) is valid for any diagonalizable tensor, a similar analysis can be made for the mean displacement tensor (and thus the diffusion tensor). In other words, D can be substituted for Q in Eq. (22) if A, B and C are also substituted with the eigenvalues of the single pore diffusion tensor. Combined, this shows exactly how the signal is influenced by pore and ensemble anisotropy in the Gaussian phase approximation.

It is instructive to understand how the special case in Eq. (19) (cylinders) is recovered from the general case in Eq. (22). In the cylindrical case, there is only one direction of symmetry corresponding to the cylinder axis, say $\hat{\mathbf{w}}$, and $A = B$, $C = 0$. The other two eigenvectors can be chosen arbitrarily with the constraint that an orthonormal coordinate system results. Thus we can take $\hat{\mathbf{u}} = \hat{\mathbf{e}} - (\hat{\mathbf{w}}\cdot\hat{\mathbf{e}})\hat{\mathbf{w}}$, where $\hat{\mathbf{e}}$ is an arbitrary unit vector, independent of $\hat{\mathbf{w}}$. This will provide a valid second eigenvector apart from a set of measure 0 where $\hat{\mathbf{e}}$ is parallel to $\hat{\mathbf{w}}$. The appropriate scatter matrix is now computed using $\langle e_\alpha e_\beta\rangle = \delta_{\alpha\beta}/3$ and independence of $\hat{\mathbf{e}}$ and $\hat{\mathbf{w}}$:

$$\begin{aligned} T^{(1)}_{\alpha\beta} &= \langle u_\alpha u_\beta\rangle \\ &= \langle e_\alpha e_\beta\rangle + \langle w_\gamma e_\gamma w_\epsilon e_\epsilon w_\alpha w_\beta\rangle - \langle e_\alpha w_\epsilon e_\epsilon w_\beta\rangle - \langle e_\beta w_\epsilon e_\epsilon w_\alpha\rangle \\ &= \delta_{\alpha\beta}/3 + \langle w_\alpha w_\beta\rangle/3 - 2\langle w_\alpha w_\beta\rangle/3 = \delta_{\alpha\beta}/3 - T^{(3)}_{\alpha\beta}/3. \end{aligned} \tag{23}$$

For the remaining scatter matrix $\mathrm{T}^{(2)}$, we rely on "completeness" by putting $\mathrm{T}^{(2)} = \mathrm{I} - \mathrm{T}^{(1)} - \mathrm{T}^{(3)}$ which then gives $\mathrm{T}^{(2)} = 2/3(\mathrm{I} - \mathrm{T}^{(3)})$ upon using Eq. (23). Inserting these results into Eq. (22) recovers Eq. (19) with $A = B = K$.

2.4. Double wave vector diffusion in curving fibers

Having established a general understanding of how microstructural and ensemble anisotropy combine in the double wave vector diffusion weighted signal in the Gaussian phase approximation, we

turn now to a new possible use of this experiment to measure the curvature and deflection angle of long tube-shaped pores such as myelinated axons. A possible application could be as a method to detect fiber populations with significant subvoxel curvature, such as small cortical U-fibers, or in regions of terminal branching from white matter fiber bundles.

We consider diffusion inside a long fiber of constant radius a, and in the limit where the mixing time τ and the diffusion time Δ are both much larger than a^2/D, the fiber tract can be modelled as a pack of lines in three dimensions (i.e. zero width). Then, in a voxel containing straight fiber bundles, the axons will appear approximately as straight lines with one-dimensional Gaussian diffusion, and thus Q = 0 (valid for small Δ also, c.f. Eq. (16)). On the other hand, in voxels with curving fiber populations, Q is nonzero because displacement correlations are experienced by spins whose directions of motion depend on their positions along the curving fiber. Therefore, voxels with straight or curving fiber bundles may in principle be distinguished by a nonzero value of the displacement correlation tensor, which will also allow an estimate of the curvature in the latter case, as will be demonstrated shortly. Note that the physical basis for the nonvanishing Q in this situation bears a close resemblance to exchange between two domains characterized by different diffusion parameters [4].

To be definite, consider the model curving fiber in Fig. 3. It consists of two straight segments in the directions specified by $\hat{\mathbf{n}}_1$ and $\hat{\mathbf{n}}_2$ with relative angle ψ (deflection angle), connected by a circular arc of radius R subtending an angle $\phi = \pi - \psi$. For simplicity, the entire fiber is supposed to be planar—see [35] for a somewhat similar model of a curving fiber. The diffusion problem can be solved in this case since diffusion along the fiber is one-dimensional and Gaussian. We consider in detail the two extreme cases of $D\Delta/(R\phi)^2 \gg 1$ (large curvature) and $D\Delta/(R\phi)^2 \ll 1$ (small curvature), under the condition that $D\Delta/L^2 \ll 1$, where L is the length of the fiber residing inside the voxel. Accordingly, we keep only leading terms of $D\Delta/L^2$ as $D\Delta/L^2 \to 0$ in the following calculations. We let $\tau \to 0$ in our computations, with the understanding that the condition of $\tau \gg a^2/D$ is fulfilled by working with infinitely thin tubes. The results are thus valid for $a^2/D \ll \tau \ll \Delta \ll L^2/D$.

In the first case $D\Delta/(R\phi)^2 \gg 1$, the fiber appears as two straight lines meeting at an angle ψ. The position of a diffusing spin can therefore be written in terms of the intrinsic arc length s on the fiber as

$$\mathbf{r}(t) = s(t)(\hat{\mathbf{n}}_2\theta(s(t)) - \hat{\mathbf{n}}_1\theta(-s(t))), \tag{24}$$

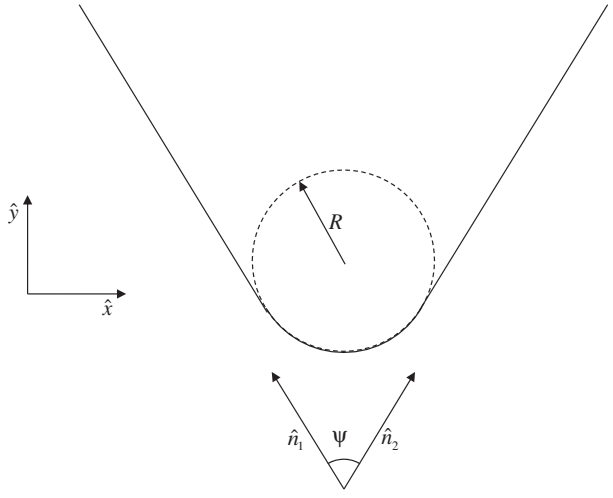

Fig. 3. Idealized model of a curving planar fiber introducing geometric parameters $1/R$ (radius of curvature), L (fiber length), ψ (deflection angle), and $\hat{\mathbf{n}}_1$ and $\hat{\mathbf{n}}_2$ (direction unit vectors).

where $s(t)$ is the position at time t of a one-dimensional random walk and $\theta(s)$ is the Heaviside step function. Using numerical subscripts to indicate time points, the displacement is

$$\begin{aligned}\mathbf{R}_1 &= \mathbf{r}_2 - \mathbf{r}_1 \\ &= \hat{\mathbf{n}}_2(s_2\theta(s_2) - s_1\theta(s_1)) - \hat{\mathbf{n}}_1(s_2\theta(-s_2) - s_1\theta(-s_1))\end{aligned} \tag{25}$$

and similarly for $\mathbf{R}_2$, and we find

$$Q_{\alpha\beta} = a(n_{1\alpha}n_{1\beta} + n_{2\alpha}n_{2\beta}) - b(n_{1\alpha}n_{2\beta} + n_{2\alpha}n_{1\beta}), \tag{26}$$

where a and b can be computed explicitly using

$$\begin{aligned}a &= \langle(s_2\theta(s_2) - s_1\theta(s_1))(s_4\theta(s_4) - s_3\theta(s_3))\rangle \\ b &= \langle(s_2\theta(s_2) - s_1\theta(s_1))(s_4\theta(-s_4) - s_3\theta(-s_3))\rangle,\end{aligned} \tag{27}$$

applicable also for $\tau > 0$. In fact, the form of Eq. (26) can be established by general arguments, since this is the only way to construct a symmetric rank 2 tensor from $\hat{\mathbf{n}}_1$ and $\hat{\mathbf{n}}_2$, which completely specify the problem in this limit, while respecting invariance under exchange of labels 1 and 2. Furthermore, since Q = 0 when $\hat{\mathbf{n}}_1 = -\hat{\mathbf{n}}_2$, we conclude $a = -b$, which is in agreement with explicit calculations using Eq. (27). Q has the eigenvectors $(\hat{\mathbf{n}}_1 + \hat{\mathbf{n}}_2)/\sqrt{2}$ (i.e. $\hat{\mathbf{y}}$ in Fig. 3) with eigenvalue $2a(1 + \hat{\mathbf{n}}_1 \cdot \hat{\mathbf{n}}_2)$ and two degenerate zero eigenvalues with eigenvectors $(\hat{\mathbf{n}}_2 - \hat{\mathbf{n}}_1)/\sqrt{2}$ (i.e. $\hat{\mathbf{x}}$ in Fig. 3) and $\hat{\mathbf{n}}_2 \times \hat{\mathbf{n}}_1$ ($\hat{\mathbf{z}}$ in Fig. 3). Note that the latter two directions can be distinguished using the diffusion tensor since its eigenvalues corresponding to directions in the xy-plane will be nonzero, in contrast to the eigenvalue associated with the z-direction, which would vanish for the planar fiber since $\Delta \gg a^2/D$. Carrying out the explicit calculations in Eq. (27), which take advantage of the fact that the process $s(t)$ is Gaussian, we find

$$Q_{yy} = -\frac{8(\sqrt{2}-1)}{3\sqrt{\pi}L}(D\Delta)^{3/2}(1 + \cos\psi) \tag{28}$$

as the only nonzero eigenvalue in this limit. Note the similarity to the S/V expression in Eq. (9) due to a similar physical origin of the two effects.

In the opposite limit of small curvature, only a small fraction of spins move from one straight segment to the other, and the main contribution to Q comes from spins diffusing on the circle arc. Here the position of the spins are conveniently parameterized in terms of $(x, y) = R(\sin(s/R), -\cos(s/R))$. It is helpful to introduce the auxiliary complex representation

$$z = Re^{is/R - i\pi/2} \tag{29}$$

and compute $\langle z_1 z_2^* \rangle$ and $\langle z_1 z_2 \rangle$, which involve the expressions $R^2\langle e^{i(s_1 \pm s_2)/R}\rangle$. Using again the Gaussian nature of s, these are readily computed and we find that both $\langle z_1 z_2^* \rangle$ and $\langle z_1 z_2 \rangle$ are real, and thus $\langle x_1 x_2 \rangle$ as well as $\langle y_1 y_2 \rangle$ are obtained immediately. Inserted into Eq. (5) we finally have

$$\begin{aligned}Q_{xx} &= -\frac{1}{2}\frac{R^3}{L}(1 - e^{-D\Delta/R^2})^2(\phi - \sin\phi) \\ Q_{yy} &= -\frac{1}{2}\frac{R^3}{L}(1 - e^{-D\Delta/R^2})^2(\phi + \sin\phi).\end{aligned} \tag{30}$$

Note that the angle $\phi = \pi - \psi$ is the angle subtended by the circular part of the fiber. The results in Eqs. (28)–(30) comply to the general scaling form

$$Q_{\alpha\beta} = \frac{R^3}{L}g_{\alpha\beta}(D\Delta/R^2, \psi), \tag{31}$$

where the asymptotic behavior of the scaling function $g_{\alpha\beta}(x, \psi)$ can be read off from Eqs. (28) and (30). Thus, the fiber directions (from the eigenvectors), deflection angles and radius of curvature $1/R$ can in principle be recovered from the behavior of Q. In a voxel of curving fibers, Q will be the sum of terms of the forms discussed above

for each of the fiber bundles. Thus as noted earlier, voxels containing curving fiber bundles can be discriminated from voxels containing straight fiber bundles by a nonzero value of the displacement correlation tensor.

3. Methods

Simulations for diffusion between parallel plates, in cylinders, and in curved fibers were performed in Matlab (The MathWorks Inc., Natick, MA) using Monte Carlo methods with at least 50,000 particles, a diffusion constant of 2 $\mu m^2/ms$, and time step $dt = 0.001$ ms. Reflecting boundaries were employed, and in all cases the mixing time τ was set to zero for simplicity.

For diffusion between parallel plates, a plate separation of $a = 5$ μm was used, diffusion times of $\Delta = 1$ and 10 ms, and 100 evenly spaced diffusion wave vectors from $q = 0$ to $q = 0.6\ \mu m^{-1}$. The double wave vector diffusion experiment was simulated only for parallel and anti-parallel wave vector directions.

For the cylinders, we generated a sample of 500 directions $\hat{\mathbf{u}}$ from a Watson distribution

$$f(\hat{\mathbf{u}}) \propto \exp(\kappa(\hat{\mathbf{u}} \cdot \hat{\mathbf{c}})^2), \tag{32}$$

a prototype axial distribution on the sphere, where κ is the concentration parameter, and a measure of the "precision" (in the sense of an inverse variance) in the main direction $\hat{\mathbf{c}}$ [33], which was taken to be the z-axis. Note that $\kappa = 0$ corresponds to the isotropic distribution on the sphere. An infinitely long cylinder of radius 2 μm was aligned with each of these directions, and the parallel and anti-parallel double wave vector diffusion experiment was simulated for a wave vector magnitude of 0.1 μm^{-1} and diffusion time $\Delta = 5$ ms. Half the hemisphere of a "24-point spherical 7-design" (a set of 24 directions) [36] was used as the basis for selecting the directions of $\mathbf{q}$, and a nonlinear least squares Levenberg–Marquardt fitting procedure supplied by Matlab was used on Eq. (6) to estimate Q. The scatter matrix T was estimated empirically by averaging over the 500 directions. The (negative) eigenvalues of Q were sorted in ascending order and the eigenvalues of the scatter matrix T sorted in descending order. This was done in order to pair the eigenvalues of T and D appropriately—according to Eq. (20), the largest eigenvalue of Q corresponds to the smallest of T, etc. The permutations obtained by this sorting were then applied to the eigenvectors of the two matrices. The second and third eigenvalues resulting in this way were averaged due to the axial symmetry of Eq. (32), and this average is henceforth referred to as the minor eigenvalue. The entire simulation was repeated for 33 values of κ ranging from 0.1 to 35.

For simulations in the curving fiber, a one-dimensional random walk representing the position along the fiber was created for each spin. This variable was then transformed to the appropriate two-dimensional cartesian coordinates according to the curvature and deflection angle of the fiber. These positions were subsequently used for calculations of the displacement correlation tensor. The whole procedure was repeated for a large number of diffusion times $\Delta = 0.1$–100 ms and geometric parameters $\psi = 5$–150° and $R = 0.1$–20 μm.

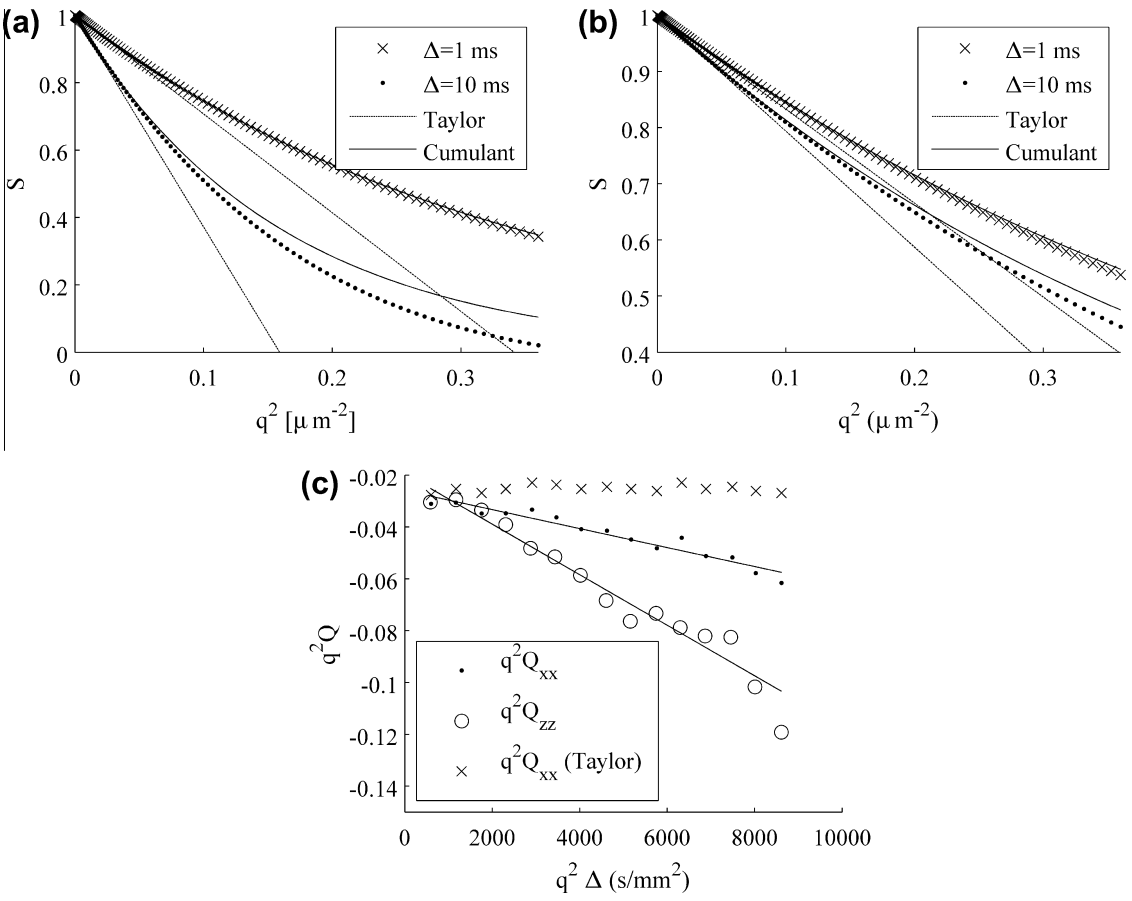

Fig. 4. The signal from spins diffusing between parallel plates compared to the cumulant expansion (solid lines) and the Taylor expansion (dashed lines): (a) parallel gradients, and (b) anti-parallel gradients. In (c), data from Fig. 7B in Komlosh et al. [13] (pig spinal cord, $\Delta = 75$ ms, $\tau = 45$ ms, $\delta = 3$ ms, and $T \approx 21$ °C) have been replotted by subtracting the logarithm of collinear and polar diffusion signals for the xx and zz components, i.e. Eq. (6). The apparently different x-axis labeling compared to Ref. [13] is due to a difference of 2π in the definition of q. Also shown with the legend "q^2Q_{xx} (Taylor)" is $1/2(S(\mathbf{q}, \mathbf{q}) - S(\mathbf{q}, -\mathbf{q}))$ for $\mathbf{q}$ in the x-direction.

4. Results and discussion

A simple illustration of the advantage of using the cumulant expansion over the Taylor expansion is shown in Fig. 4a and b, where the double wave vector diffusion signal from spins diffusing between parallel plates is shown as a function of q^2. Simulation results are plotted for two diffusion times, and for the parallel (a) and anti-parallel (b) wave vectors. It is clear from Fig. 4 that the cumulant expansion provides a better approximation of the double wave vector diffusion signal from diffusion between parallel plates for larger wave vectors. The cumulant expansion offers the best approximation for small diffusion times, where the effects of restrictions are the smallest, and for parallel gradients. The latter is a consequence of the fact that the net effective diffusion attenuation is larger for the parallel case. The Taylor expansion begins to deviate already from $q \gtrsim 0.2\ \mu m^{-1}$ ($qa \gtrsim 1$), whereas the cumulant expansion is accurate at least up to $q \gtrsim 0.3\ \mu m^{-1}$ ($qa \gtrsim 1.5$) and often much longer. This is to be compared to values in experiments. For example, Ref. [13] uses a maximum of $q \approx 0.3\ \mu m^{-1}$ in experiments in porcine spinal cord, and assuming an axon radius of $a \approx 6\ \mu m$, qa enters the regime in which the cumulant expansion is more accurate. This is also the case for the experiments in radish in Ref. [14] where qa is of the order of 2.8. A more practical application is shown in Fig. 4c, where pig spinal cord data read off from Fig. 7b in [13] have been replotted in terms of Eq. (6) for $Q_{xx}q^2$ and $Q_{zz}q^2$ versus Δq^2. The use of the cumulant expansion (difference of log signals) allows a clear linear dependence to be easily identified from the data. Also shown is the data plotted instead as the difference of signals (i.e. no logarithms), where no systematic trend is revealed. The slopes in Fig. 4c correspond to Q_{xx} and Q_{zz}, and assuming an estimate of the intracellular water diffusion constant in the range $0.3\ \mu m^2/ms \leqslant D \leqslant 2\ \mu m^2/ms$ ($T \approx 21\ ^\circ C$) in Eq. (16) for Q_{xx}, this provides a realistic estimate of the axon radius $4\ \mu m \lesssim a \lesssim 9\ \mu m$ in pig spinal cord white matter [37]. It is interesting to observe that the absolute value of the slope of Q_{zz} is larger. The nonvanishing value of Q_{zz} could be due to a slight misalignment of the spinal cord with the z-axis, or it could be a signature of real correlations in the displacement in the direction along the fibers—in the intracellular or extracellular space. If there are restrictions along this axis, the absolute value of Q_{zz} could become larger than Q_{xx}, if the restriction scale a is larger in the former direction, and depending on the value of $D\Delta$: the absolute value of Tr(Q) is 0 for $\Delta = 0$, and approaches a number on the order of a^2 asymptotically—the crossover occurs approximately when $D\Delta \sim a^2$. Thus, for a compartment with restriction lengths a_x and a_z, with $a_x \ll a_z$, we can have $Q_{zz} < Q_{xx}$ when $D\Delta \sim a_x^2$ and $Q_{xx} < Q_{zz}$ when $D\Delta \sim a_z^2$.

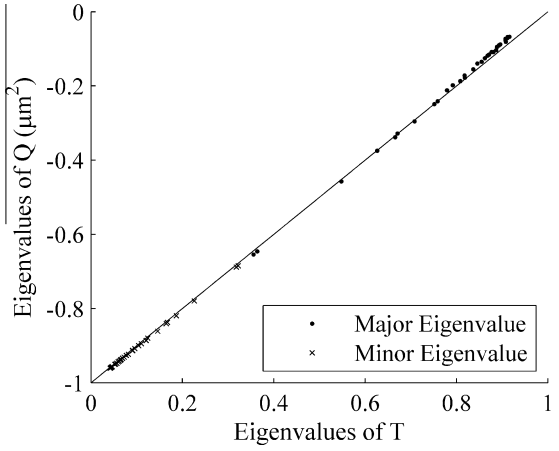

Fig. 5. Eigenvalues of Q versus eigenvalues of T for various choices of the concentration parameter κ in the Watson distribution Eq. (32).

In Fig. 5, simulation results from distributions of identical cylinders are shown. Here the sorted eigenvalues of Q have been plotted against the eigenvalues of T, the scatter matrix, and the solid line represents the theoretical expectations according to Eq. (20). The main eigenvectors of Q and T were highly aligned, in terms of the angle θ between them, we found $\langle\cos\theta\rangle = 0.94 \pm 0.07$ (standard deviation). The reliability of the primary eigenvectors in identifying the z-axis can also be characterized by the mean resultant vector, $1/N\sum_k^N \hat{\mathbf{n}}_k$, where $\hat{\mathbf{n}}_k$ are the normalized eigenvectors of Q, and the sum is over the different κ-values. The mean resultant vector for the primary eigenvector of the displacement correlation tensor was at an angle of 2.7° with the z-axis and had a length of 0.67. The corresponding numbers for the scatter matrix were 1.5° and 0.97. The recovery of the scatter matrix in a distribution of identical cylinders is thus very robust, as evidenced by the similarity between the simulation results and theory in Fig. 5, along with the small scatter in angles around 0. In a practical experiment, this would allow one to extract second-order information of the orientational distribution, along with the cylinder radius. In order to garner similar information for a general pore shape, one would need independent information about the orientation distribution of the pores. Alternatively, additional information can be obtained by acquiring measurements of the time dependence of Q. If the pore shape and thus the pore anisotropy in terms of A, B and C is known, the elements of the principal direction scatter matrices can be extracted by fitting the data points to Eqs. (6) and (22).

Note that if the cumulant expansion is continued to higher order terms, the resulting signal will become sensitive to higher moments of the orientational distribution function[1] allowing more detailed information about ensemble anisotropy to be extracted. This in turn requires higher diffusion weighting, and thus greater angular resolution requires not only finer angular sampling, but also higher q values—not withstanding the counteracting effects of decreased signal to noise. This remark applies equally to standard diffusion experiments.

When the mixing time τ and diffusion time Δ become large compared to the time taken to diffuse across the diameter of the cylinder, a single straight cylinder will appear as a line with Q = 0. This provides the justification for approximating axons as one-dimensional lines, the starting point in the analysis of the double wave vector diffusion experiment in curved fibers. Here we begin by giving an impression of the data variation by plotting in Fig. 6a Q versus diffusion time for a subset of the radii of curvature as given on the figure and a deflection angle of 10°. In Fig. 6b, we show the collapse of the data for *all* radii and three values of ψ (10°, 100° and 150° from bottom to top), and thus the tremendous simplification offered by the scaling form Eq. (31), by plotting $Q_{z\beta}L/R^3$ versus $D\Delta/R^2$. The collapse of the entire data set in Fig. 6b provides strong support for the proposed scaling form of the signal in a curved fiber.

In Fig. 7a, we demonstrate the agreement with the theoretical prediction in Eq. (28) for large diffusion times, by replotting Fig. 6b on a double logarithmic scale, along with the theoretical form as a dashed line. Even though Eq. (28) was derived in an asymptotic regime of large $D\Delta/R^2$, it provides good agreement already from $D\Delta/R^2 \gtrsim 1$ as evident from the figure. To illustrate the dependence on deflection angle, theoretical and numerical results are plotted in Fig. 7b as a function of deflection angle, for $R = 2\ \mu m$ and a few values of the diffusion time Δ (40, 60, 80 and 100 ms from top to bottom). The simulations agree well with the theory here also.

[1] Jespersen, Leigland, Cornea and Kroenke, work in progress.

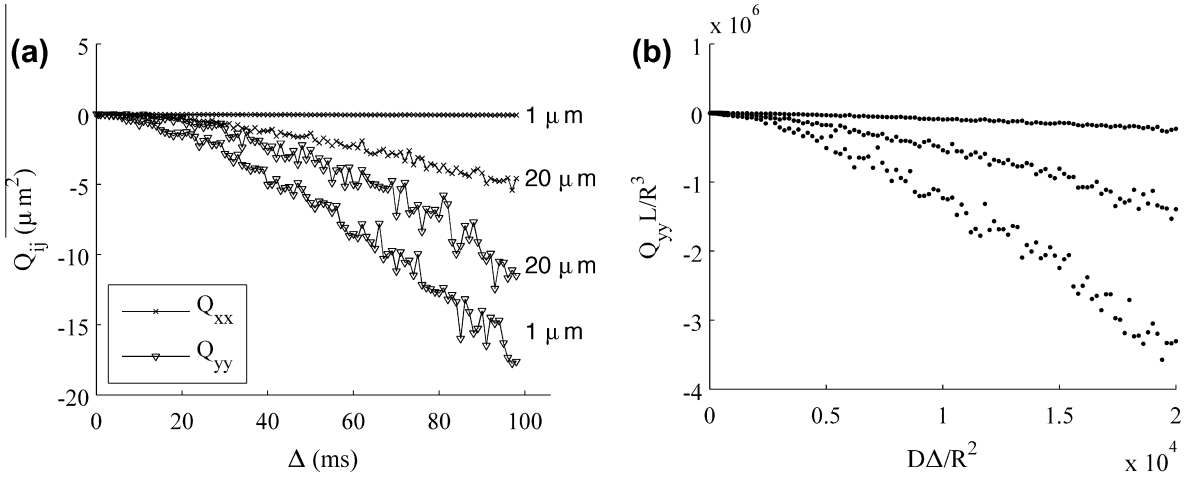

Fig. 6. A subset of the simulation results for Q_{xx} and Q_{yy} corresponding to $R = 1$ μm and 20 μm (as noted at the right end of the curves) and $\psi = 10°$ in the curving fiber are shown versus diffusion time in (a) to illustrate the variability in the data. In (b) the entire data set (all radii) has been plotted as $Q_{\alpha\beta}L/R^3$ versus $D\Delta/R^2$ for $\psi = 10°$, 100° and 150° (bottom to top) to illustrate the collapse supporting the scaling form in Eq. (31).

Finally, plots in the regime of low diffusion times are shown in Fig. 8, along with theoretical curves. In Fig. 8a and b $Q_{\alpha\beta}L/R^3$ is shown against $D\Delta/R^2$ for $\psi = 5°$ (a) and $\psi = 50°$ (b). Fig. 8c shows displacement correlations as a function of deflection angle for $R = 20$ μm and $\Delta = 19.6$ ms. This regime is quite noisy and difficult to assess numerically. This is due to the fact that it is a small effect easily corrupted by contributions originating from spins in the linear segments. For very small values of $D\Delta/R^2$ there is a reasonable agreement between theory and simulation in Fig. 8a and b, but as $D\Delta/R^2$ increases, the ability of the theoretical expressions to approximate the data rapidly deteriorates, and this is due to the increasing importance of spins migrating between the circular and linear parts of the fiber. The theoretical approximation essentially treats this regime as diffusion on a circle [35] with an initial non-zero density only at the circle arc subtended by ϕ. However, the real pore shape does not curve beyond this circle arc, and thus the theoretical expression overestimates the displacement correlations for spins probing the linear parts of the fiber. In fact, a numerical integration of the averages in Eq. (5) using a Gaussian diffusion propagator yields excellent agreement with the data points (not shown). Due to the smallness of the signal, this regime is presumably going to be challenging to assess experimentally. Adapting the voxel size so as to maximize the volume fraction occupied by the curving part of the fiber would be essential.

The presence of a curving fiber, along with an estimate of the radius of curvature and deflection angle can thus in principle be inferred from the eigenvectors of Q. Several aspects complicate this in practice. The most obvious ones are the deviations of real fiber tracts from tubes, and the presence of extra-cellular water. This will imply that Q is not zero for straight fibers, even for $D\tau \gg a^2$, but perhaps a sufficiently low value of Tr(Q) can be used as a threshold to indicate the presence of a curving fiber, or a more refined probabilistic approach could be pursued by including information from other MR experiments. It may also be that a careful choice of pulse sequence parameters, especially the time parameters, can ameliorate this problem since the contributions to Q from compartments of different sizes depend sensitively on τ and Δ. Note that to the extent that extracellular diffusion can be approximated as effectively Gaussian diffusion, as assumed in several current theoretical models [38–42], it does not contribute to Q, but may serve to lower the signal to noise ratio in the estimate of Q. Alternatively, it may be necessary to employ intracellular markers such as NAA [43]—this seems not to be an unreasonable requirement, given the complex geometrical information one is trying to extract from the diffusion signal.

All the results presented here were derived under the narrow pulse regime, c.f. Eq. (1). While this has the advantage of facilitating a clear physical picture, it represents a constraint which is fre-

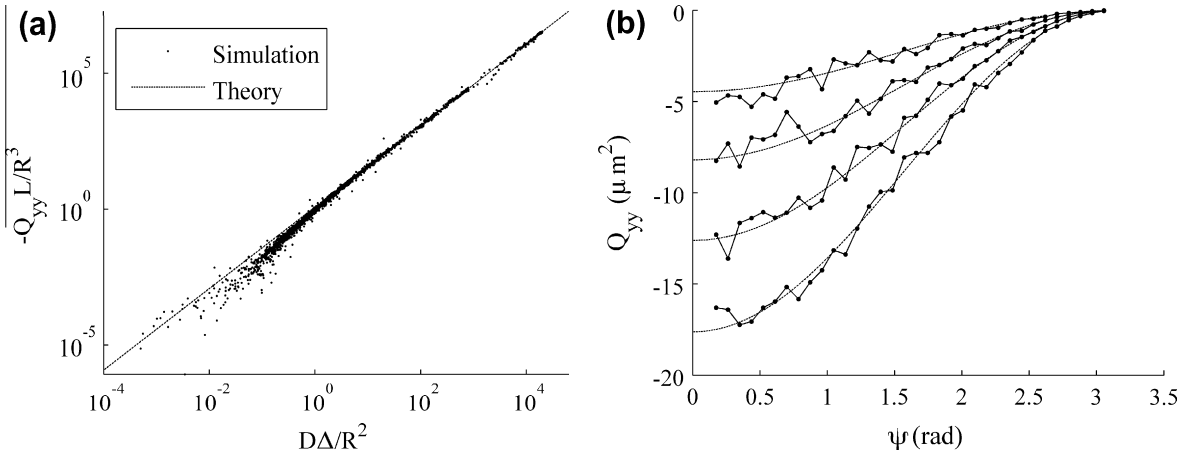

Fig. 7. (a) $Q_{yy}L/R^3$ versus $D\Delta/R^2$ for a deflection angle of 20° on a log–log plot, and (b) Q_{yy} versus deflection angle ψ for various choices of diffusion time Δ (40, 60, 80 and 100 ms from top to bottom). Theoretical predictions are shown as lines.

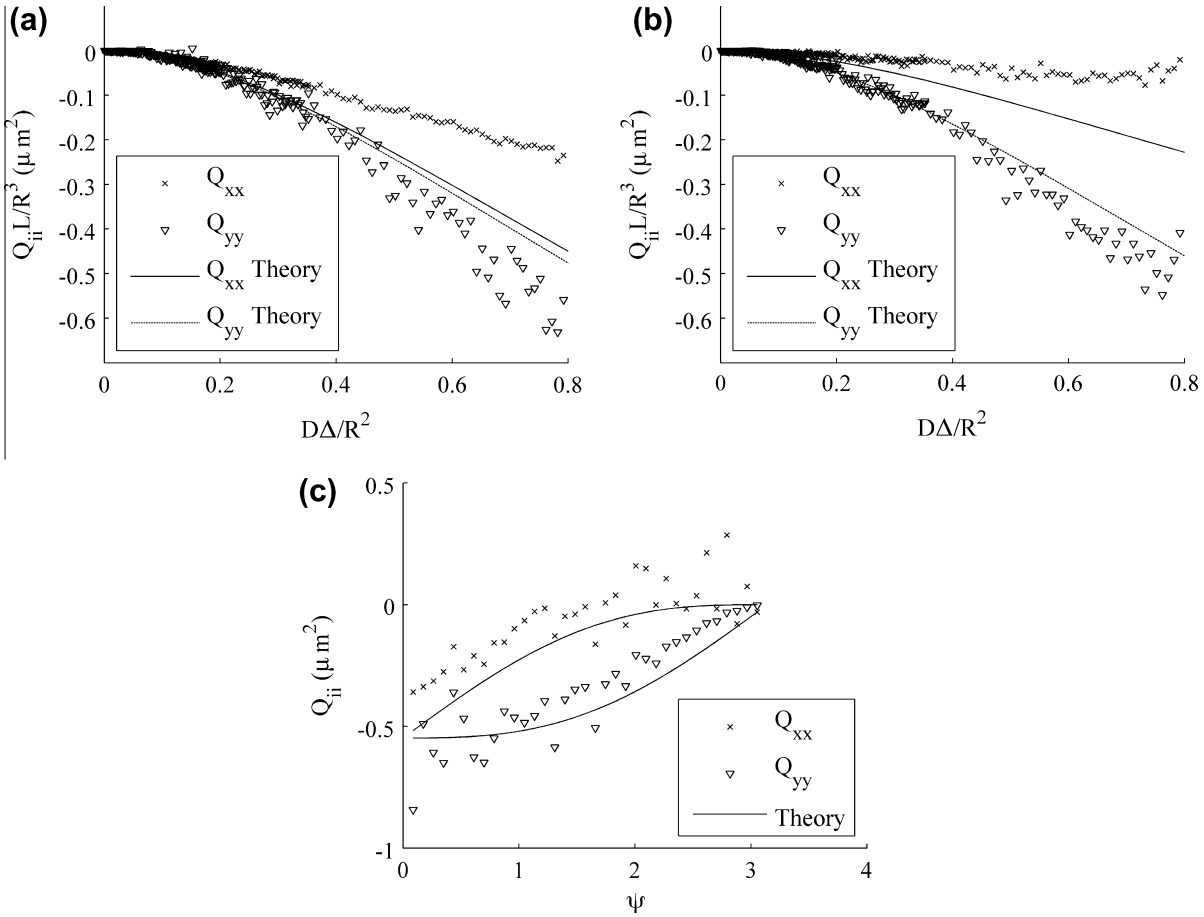

Fig. 8. $Q_{\alpha\beta}L/R^3$ versus $D\Delta/R^2$ for $\psi = 5°$ (a) and for $\psi = 50°$ (b). In (c) the dependence of Q on deflection angle for $R = 20$ μm and $\Delta = 19.6$ ms is shown. Theoretical predictions are shown as lines.

quently challenging to meet in practice. It therefore remains to be analyzed how violations of these idealized assumptions affect the results presented in this work. The framework presented in [20] would presumably be well-suited to address these questions.

5. Conclusion

We presented a new analysis of the Gaussian phase approximation of the double wave vector diffusion experiment in the narrow pulse limit. We focused in particular on the displacement correlation tensor Q, discussing its physical interpretation and properties in some depth. A notable result was an expression relating the short time behavior of the displacement correlation tensor to the surface to volume ratio of the pore space, analogous to the classical result for the diffusion coefficient [26,27]. We derived a simple and compact expression showing how the displacement correlation tensor embodies information about pore shape and ensemble properties in collections of cylinders, and for completely general pore shapes. In the last part, we addressed the ability of the double wave vector diffusion experiment to detect fiber curvature and deflection angle by analyzing its behavior in an idealized model of a curving fiber. We derived exact expressions in the limits of long and short diffusion times, and noted the potential for detecting and characterizing high curvature fiber populations.

Acknowledgments

Both authors are grateful to the Danish National Research Foundation for financial support, and to our colleagues Brian Hansen and Leif Østergaard for discussions. SNJ expresses gratitude toward Søren Frimann and Chris Ørum for technical assistance.

References

[1] D.G. Cory, A.N. Garroway, J.B. Miller, Applications of spin transport as a probe of local geometry, Polym. Prepr. (Am. Chem. Soc. Div. Polym. Chem.) 31 (1990) 149.
[2] Y. Cheng, D.G. Cory, Multiple scattering by NMR, J. Am. Chem. Soc. 121 (1999) 7935–7936.
[3] P.T. Callaghan, A.A. Khrapitchev, Time-dependent velocities in porous media dispersive flow, Mag. Reson. Imaging 19 (2001) 301–305.
[4] P.T. Callaghan, B. Manz, Velocity exchange spectroscopy, J. Magn. Reson. 106 (1994) 260–265.
[5] A. Jerschow, N. Müller, Suppression of convection artifacts in stimulated-echo diffusion experiments. Double-stimulated-echo experiments, J. Magn. Reson. 125 (1997) 372–375.
[6] P.P. Mitra, Multiple wave-vector extensions of the NMR pulsed-field-gradient spin-echo diffusion measurement, Phys. Rev. B 51 (1995) 15074–15078.
[7] M.A. Koch, J. Finsterbusch, Multiple wave vector diffusion experiments on restricted diffusion, in: Proceedings ISMRM, vol. 13, 2005.
[8] M.E. Komlosh, R.Z. Freidlin, F. Horkay, Y. Asaf, P.J. Basser, Detection of microscopic anisotropy in gray matter using d-PGSE, in: Proceedings ISMRM, vol. 13, 2005.
[9] M.A. Koch, J. Finsterbusch, Double wave vector diffusion weighting in the human corticospinal tract in vivo, in: Proceedings ISMRM, vol. 16, 2008.
[10] N. Shemesh, E. Özarslan, P.J. Basser, Y. Cohen, Measuring small compartmental dimensions with low-q angular double-PGSE NMR: the effect of experimental parameters on signal decay, J. Magn. Reson. 198 (2009) 15–23.
[11] E. Özarslan, N. Shemesh, P.J. Basser, A general framework to quantify the effect of restricted diffusion on the NMR signal with applications to double pulsed field gradient NMR experiments, J. Chem. Phys. 130 (2009) 104702.
[12] N. Shemesh, E. Özarslan, A. Bar-Shir, P.J. Basser, Y. Cohen, Observation of restricted diffusion in the presence of a free diffusion compartment: single- and double-PFG experiments, J. Magn. Reson. 200 (2009) 214–225.
[13] M.E. Komlosh, F. Horkay, R.Z. Freidlin, U. Nevo, Y. Assaf, P.J. Basser, Detection of microscopic anisotropy in gray matter and in a novel tissue phantom using double pulsed gradient spin echo MR, J. Magn. Reson. 189 (2007) 38–45.

[14] M.A. Koch, J. Finsterbusch, Compartment size estimation with double wave vector diffusion-weighted imaging, Magn. Reson. Med. 60 (2008) 90–101.
[15] M.E. Komlosh, M.J. Lizak, F. Horkay, R.Z. Freidlin, P.J. Basser, Observation of microscopic diffusion anisotropy in the spinal cord using double-pulsed gradient spin echo MRI, Magn. Reson. Med. 59 (2008) 803–809.
[16] T. Weber, C.H. Ziener, T. Kampf, V. Herold, W.R. Bauer, P.M. Jakob, Measurement of apparent cell radii using a multiple wave vector diffusion experiment, Magn. Reson. Med. 61 (2009) 1001–1006.
[17] E. Özarslan, P.J. Basser, MR diffusion – "diffraction" phenomenon in multi-pulse-field-gradient experiments, J. Magn. Reson. 188 (2007) 285–294.
[18] N. Shemesh, Y. Cohen, The effect of experimental parameters on the signal decay in double-PGSE experiments: negative diffractions and enhancement of structural information, J. Magn. Reson. 195 (2008) 153–161.
[19] N. Shemesh, E. Özarslan, P.J. Basser, Y. Cohen, Detecting diffusion–diffraction patterns in size distribution phantoms using double-pulsed field gradient NMR: theory and experiments, J. Chem. Phys. 132 (2010) 034703.
[20] E. Özarslan, P.J. Basser, Microscopic anisotropy revealed by NMR double pulsed field gradient experiments with arbitrary timing parameters, J. Chem. Phys. 128 (2008) 154511.
[21] E. Özarslan, Compartment shape anisotropy (CSA) revealed by double pulsed field gradient MR, J. Magn. Reson. 199 (2009) 56–67.
[22] A.V. Barzykin, Exact solution of the Torrey–Bloch equation for a spin echo in restricted geometries, Phys. Rev. B 58 (1998) 14171–14174.
[23] D.S. Grebenkov, Analytical solution for restricted diffusion in circular and spherical layers under inhomogeneous magnetic fields, J. Chem. Phys. 128 (2008) 134702.
[24] J. Finsterbusch, M.A. Koch, A tensor approach to double wave vector diffusion-weighting experiments on restricted diffusion, J. Magn. Reson. 195 (2008) 23–32.
[25] M. Lawrenz, M.A. Koch, J. Finsterbusch, A tensor model and measures of microscopic anisotropy for double-wave-vector diffusion-weighting experiments with long mixing times, J. Magn. Reson. 202 (2010) 43–56.
[26] P.P. Mitra, P.N. Sen, L.M. Schwartz, P. Le Doussal, Diffusion propagator as a probe of the structure of porous media, Phys. Rev. Lett. 68 (1992) 3555–3558.
[27] P.P. Mitra, P.N. Sen, L.M. Schwartz, Short-time behavior of the diffusion coefficient as a geometrical probe of porous media, Phys. Rev. B 47 (1993) 8565–8575.
[28] P.T. Callaghan, Principles of Nuclear Magnetic Resonance Microscopy, Clarendon Press, Oxford, England, 1991.
[29] H. Risken, The Fokker–Planck Equation: Methods of Solution and Applications, Springer-Verlag, Berlin, 1984.
[30] J. Stepišnik, A new view of the spin echo diffusive diffraction in porous structures, Europhys. Lett. 60 (2002) 453.
[31] J.H. Jensen, J.A. Helpern, A. Ramani, H. Lu, K. Kaczynski, Diffusional kurtosis imaging: the quantification of non-gaussian water diffusion by means of magnetic resonance imaging, Magn. Reson. Med. 53 (2005) 1432–1440.
[32] G.B. Arfken, H.J. Weber, Mathematical Methods for Physicists, vol. 6, Elsevier, Boston, 2005.
[33] N.I. Fisher, T. Lewis, B.J.J. Embleton, Statistical Analysis of Spherical Data, Cambridge University Press, 1987.
[34] S.N. Jespersen, L.A. Leigland, A. Cornea, C.C. Kroenke, The diffusion tensor reveals gray matter architecture, in: Proceedings ISMRM, Honolulu, Hawaii, vol. 17, 2009 (ote a misprint: $v/2$ should be v).
[35] E. Özarslan, C.G. Koay, P.J. Basser, Remarks on q-space mr propagator in partially restricted, axially-symmetric, and isotropic environments, Magn. Reson. Imaging 27 (2009) 834–844.
[36] R.H. Hardin, N.J.A. Sloane, McLaren's improved snub cube and other new spherical designs in three dimensions, Discrete Comput. Geom. 15 (1996) 429–441 (Coordinates for spherical designs can be downloaded from <http://www2.research.att.com/njas/sphdesigns/index.html>).
[37] Y. Assaf, T. Blumenfeld-Katzir, Y. Yovel, P.J. Basser, AxCaliber: a method for measuring axon diameter distribution from diffusion MRI, Magn. Reson. Med. 59 (2008) 1347–1354.
[38] Y. Assaf, R.Z. Freidlin, G.K. Rohde, P.J. Basser, New modeling and experimental framework to characterize hindered and restricted water diffusion in brain white matter, Magn. Reson. Med. 52 (2004) 965–978.
[39] S.N. Jespersen, C.D. Kroenke, L. Østergaard, J.J.H. Ackerman, D.A. Yablonskiy, Modeling dendrite density from magnetic resonance diffusion measurements, NeuroImage 34 (2007) 1473–1486.
[40] S.N. Jespersen, C.R. Bjarkam, J.R. Nyengaard, M.M. Chakravarty, B. Hansen, T. Vosegaard, L. Østergaard, D. Yablonskiy, N.C. Nielsen, P. Vestergaard-Poulsen, Neurite density from magnetic resonance diffusion measurements at ultrahigh field: comparison with light microscopy and electron microscopy, NeuroImage 49 (2010) 205–216.
[41] R.V. Mulkern, S.J. Haker, S.E. Maier, On high b diffusion imaging in the human brain: ruminations and experimental insights, Magn. Reson. Imaging 27 (2009) 1151–1162.
[42] D.A. Yablonskiy, A.L. Sukstanskii, Theoretical models of the diffusion weighted MR signal (2010), doi:10.1002/nbm.1520.
[43] C.D. Kroenke, J.J. Ackerman, D.A. Yablonskiy, On the nature of the NAA diffusion attenuated MR signal in the central nervous system, Magn. Reson. Med. 52 (2004) 1052–1059.